Unsteady models for the nonlinear evolution of the mixing layer

Eckart Meiburg,* Paul K. Newton, Narayanan Raju, and Greg Ruetsch

Department of Aerospace Engineering, University of Southern California, Los Angeles, California 90089-1191
(Received 22 August 1994; revised manuscript received 3 February 1995)

We investigate several unsteady two-dimensional models of increasing complexity for the nonlinear evolution of the temporally growing mixing layer. In the simplest model, we use a subharmonically perturbed point vortex row which serves initially to identify certain key dynamical and kinematic aspects of the transition process, in which small scales in the flow are rapidly generated as a result of the vortex pairing process. A slightly more realistic vortex blob model is used at the next level. Finally, Navier-Stokes calculations are performed in order to identify which features are artifacts of the earlier models, and which ones are likely to be inherent to the physics. An important kinematic aspect of the transition, present in all of the models for small subharmonic perturbations, is a change in the topology of the streamline pattern when viewed in a rotating reference frame. This topological change contributes to the formation of spiral arm structures seen in other work and consequently to the intense production of small scales. For larger subharmonic perturbation amplitudes, this effect does not occur. We attempt to establish a connection between the aspects of our two-dimensional models and the findings of other authors in three-dimensional computations and experiments.

PACS number(s): 47.27.Cn

I. INTRODUCTION

Experimental and computational research carried out in recent years has demonstrated the existence of a certain stage in the evolution of the plane mixing layer during which the production of small scales increases rapidly, thereby leading to the emergence of turbulent flow. This process is typically accompanied by a dramatic increase in the mixing rates of the two streams, hence this event has become known as the "mixing transition" in the literature (Konrad [1] and Breidenthal [2]).

Experimental work by Huang and Ho [3] as well as by Zohar [4] indicates that this generation of small scales is correlated to the growth of subharmonic streamwise perturbations and to the resulting merging of spanwise coherent structures, which is known to be the dominant growth mechanism of plane mixing layers (Winant and Browand [5]). Employing the peak-valley counting technique, they observe that fine scale turbulence occurs first in the cores of the streamwise vortices that are known to form in the braid region in between the spanwise rollers (Bernal [6], Corcos and Lin [7], Lin and Corcos [8], Bernal and Roshko [8], Ashurst and Meiburg [10], Lasheras and Choi [11]). Furthermore, they find that the small scales occur first in between pairing spanwise vortices, rather than in between vortex pairs. Hence, they speculate that the strain field in between merging vortices triggers the transition by acting on the streamwise structures.

---

*Corresponding author. Permanent address: Department of Aerospace Engineering, University of Southern California, Los Angeles, CA 90089-1191. FAX: 213-740-7774. E-mail: eckart@spock.usc.edu

Moser and Rogers [12,13] present direct Navier-Stokes simulations for a temporally growing three-dimensionally evolving plane mixing layer that are consistent with the above experimental findings. Their calculations of mixing layers undergoing up to three pairings show the pairing process to inhibit the growth of infinitesimal three-dimensional (3D) perturbations. At the same time, the authors observe the formation of thin sheets of spanwise vorticity that are subject to a secondary rollup instability. Their calculations furthermore exhibit the formation of spiral arms of the spanwise vorticity, similarly to the findings of Martel, Mora, and Jimenez [14]. Moser and Rogers furthermore report that the long time evolution of finite amplitude three-dimensional perturbations is surprisingly similar to that of infinitesimal perturbations, implying that the three-dimensional evolution is to a large extent dictated by the evolution of the underlying two-dimensional flow.

In summary, the existing body of knowledge indicates the importance of both the vortex pairing process resulting from streamwise subharmonic perturbations and the streamwise vorticity generation in the braid region between the Kelvin-Helmholtz rollers. The conceptually simple scenario described by Bernal and Roshko [9] for the evolution of initially weak steamwise braid vorticity is based on the deformation that a passive wavy spanwise line element undergoes in the steady flow field of a row of Kelvin-Helmholtz vortices. The main goal of the present investigation, then, is to extend the Bernal-Roshko model to the temporally evolving two-dimensional subharmonically perturbed mixing layer. In other words, we aim to describe both qualitatively and quantitatively the deformation of passive line elements in subharmonically evolving mixing layers, in order to obtain insight into the mechanisms that govern the evolution of initially weak streamwise vorticity. Put differently, our emphasis lies in

analysis of simple two-dimensional flow models for information about three-dimensional phenomena.

To elucidate the way in which a subharmonic perturbation can enhance the production of two- and three-dimensional small scales, we first employ a simple two-dimensional streamwise periodic mixing layer model discretized into point vortices or finite core vortex blobs, and perturbed in a subharmonic fashion. We let the vorticity field evolve under the assumption of inviscid dynamics, based on the experimental and computational observation that the mixing transition occurs beyond a threshold Reynolds number range, i.e., that it is an essentially inviscid phenomenon (Koochesfahani and Dimotakis [15], Moser and Rogers [13]). Subsequently, we present results of Navier-Stokes simulations to further clarify which aspects of the point vortex and vortex blob models are likely to be artifacts of the approximation, and which are inherent in the physics.

In particular, Sec. II contains the results for the inviscid vortex models. We focus on two distinct flow regions. The first one is the region surrounding the vortex centers where fluid particles undergo both periodic and quasi-periodic motion, the details of which are addressed in Appendix A. Further from the vortex centers is a chaotic region which we study by means of Poincaré maps and calculations of fluid stretching rates, related to the Lyapunov exponent. By examining the topology of the streamline pattern in a rotating reference frame, we describe a topological transition that we believe is primarily responsible for spiral arm structures and small scale development. This topological transition exists for both point vortices and vortex blobs. Section III analyzes a series of Navier-Stokes simulations. The stretching and folding of interfaces is described and compared with the preceding sections and, again, the topological transition seen in the preceding two models is identified. Finally, in Sec. IV we compare some of our findings with results seen in other work.

II. INVISCID VORTEX MODELS

A. Point vortices

We begin our analysis of transition processes in mixing layers by considering the simplest model of the flow field that exhibits the same qualitative behavior as more detailed simulations. This approach offers several advantages. First, it is easier to determine potentially relevant mechanisms for the transition processes, whose existence in more realistic simulations can then later be checked. In addition, if these mechanisms persist in different models of the flow, this indicates their robustness, i.e., that they are not an artifact of the simulation method. In light of this, we first simulate the subharmonic pairing dynamics by representing the individual vortices in the mixing layer as point vortices.

1. Flow simulation

The shear layer is initially configured as a row of point vortices of equal strength Γ evenly distributed along the horizontal axis $y = 0$, at positions $x = \cdots -1.5,$

$-0.5, 0.5, 1.5, \ldots$ (Fig. 1). To simulate a subharmonic pairing event, we displace each vortex a distance X_{pert} along the x axis in alternating directions. The flow field can then be advanced in time by moving the point vortices with the velocity $(\dot{x}_{\text{vor}}, \dot{y}_{\text{vor}})$ induced upon them by all other vortices. The symmetry properties of the flow lead to

$$\dot{x}_{\text{vor}} = \frac{-\Gamma}{4} \frac{\sinh(2\pi y_{\text{vor}})}{\cosh(2\pi y_{\text{vor}}) - \cos(2\pi x_{\text{vor}})} , \qquad (2.1)$$

$$\dot{y}_{\text{vor}} = \frac{\Gamma}{4} \frac{\sin(2\pi x_{\text{vor}})}{\cosh(2\pi y_{\text{vor}}) - \cos(2\pi x_{\text{vor}})} , \qquad (2.2)$$

where x_{vor} and y_{vor} refer to the location of the point vortex in the interval $0 < x < 1$. The influence of the second vortex within the pair, as well as of all periodic images, is accounted for implicitly by the above equations. We integrate the point vortex positions by means of a standard fourth-order Runge-Kutta scheme. The time-dependent flow field has the form of corotating vortex pairs which are a distance $D = (1 - 2 \times X_{\text{pert}})$ apart from each other when crossing the x axis. The related time-dependent streamline pattern is shown in Fig. 2 at several times over half a period. As expected, the two classes of symmetry points, $(0,0), (\pm 1, 0)$, remain free stagnation points for all times. The stagnation points at $x = \cdots -3, -1, 1, 3, \ldots$ remain connected at all times by separatrices whose shapes vary periodically in time. Embedded in the enclosed region are the two point vortices rotating around each other, as shown by the rotating figure eight pattern. The value of X_{pert} represents the strength of the subhar-
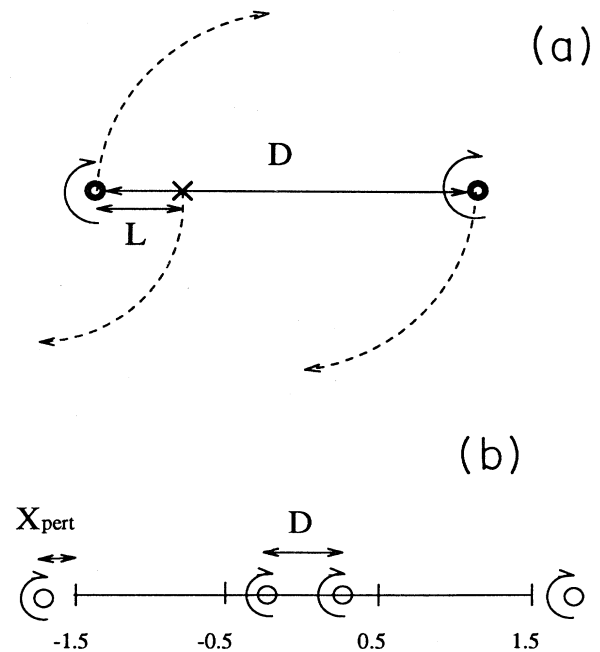

FIG. 1. Schematic diagram of a rotating vortex pair a distance D apart, and a particle starting a distance L from the left vortex.
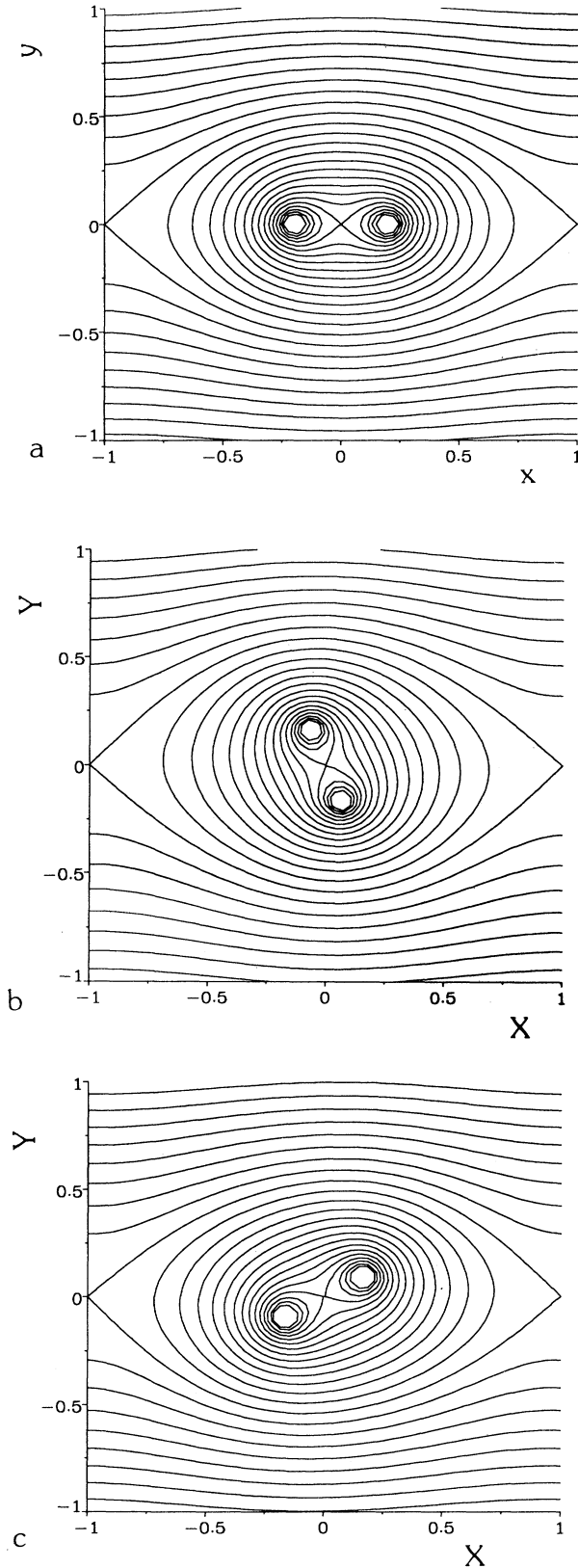
FIG. 2. Time-dependent streamline pattern for the subharmonically perturbed point vortex row $(X_{\text{pert}} = 0.3)$ at times $t = 0.0, 0.57$, and 1.14, i.e., after $0, 0.2$, and 0.4 periods.

monic mode relative to the fundamental mode; as X_{pert} increases, the subharmonic mode is stronger.

It is worthwhile to point out the similarity between this flow field and the perturbed flow fields considered by Beigie, Leonard, and Wiggins [16] and Rom-Kedar, Leonard, and Wiggins [17]. In our model, the periodic perturbation arises naturally from the oscillations of the neighboring pairs, while theirs is imposed explicitly.

The motion of Lagrangian particles can be evaluated along with that of the point vortices according to

$$\dot{x} = \frac{-\Gamma}{4} \frac{\sinh[\pi(y - y_{\text{vor}})]}{\cosh[\pi(y - y_{\text{vor}})] - \cos[\pi(x - x_{\text{vor}})]}$$

$$- \frac{\Gamma}{4} \frac{\sinh[\pi(y + y_{\text{vor}})]}{\cosh[\pi(y + y_{\text{vor}})] - \cos[\pi(x + x_{\text{vor}})]} , \quad (2.3)$$

$$\dot{y} = \frac{\Gamma}{4} \frac{\sin[\pi(x - x_{\text{vor}})]}{\cosh[\pi(y - y_{\text{vor}})] - \cos[\pi(x - x_{\text{vor}})]}$$

$$+ \frac{\Gamma}{4} \frac{\sin[\pi(x + x_{\text{vor}})]}{\cosh[\pi(y + y_{\text{vor}})] - \cos[\pi(x + x_{\text{vor}})]} . \quad (2.4)$$

The above equations are integrated using a fourth-order Runge-Kutta scheme. The flow field causes the vortices to move in closed orbits whose periods depend on the magnitude of the subharmonic perturbation. This periodicity can be used to reduce the number of computations in the following way. The location of the vortices is computed and stored for all time steps up to one period. These values are then used to compute the fluid particle velocity for successive periods. From these computations, we find two distinct regions in the flow field in terms of the particle behavior. Around each vortex center is a nearly circular region in which particles undergo periodic and quasiperiodic motion. The size of this region has a characteristic radius L_T. Asymptotic estimates of L_T and an extensive characterization of the periodic and quasiperiodic motion observed in this region are presented in Appendix A.

2. Chaotic regions

Particles that are initially placed a distance $L > L_T$ from a vortex center typically undergo a chaotic motion, shown in the series of Poincaré sections of Fig. 3. The sections are computed by choosing 80 initial conditions and iterating over 100 vortex periods. In order to eliminate any artifacts due to the particular choice of the initial conditions, only data beyond the first ten periods are shown. Displayed in Fig. 3 are plots representing increasing strength of the subharmonic mode, with X_{pert} ranging from 0.1 to 0.4. In the case of the weakest subharmonic component $(X_{\text{pert}} = 0.1)$, the periodic and quasiperiodic zones around the vortex centers are evident, otherwise no particular structure is seen. Particles starting far enough away from the vortex centers enter into a chaotic region and, in general, can easily escape the window $-1 \le x \le 1$. As the subharmonic mode becomes stronger, island structures above and below the center line appear, as shown for $X_{\text{pert}} = 0.25, 0.3, 0.35,$
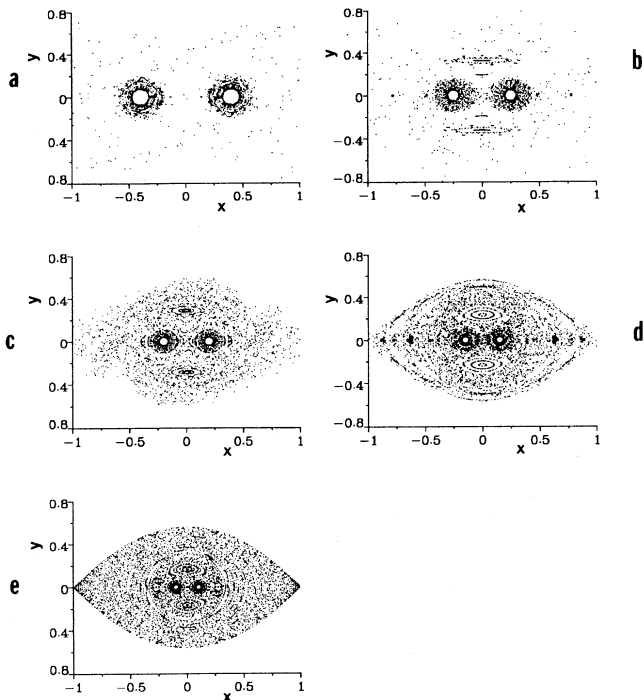
FIG. 3. Poincaré sections for point vortex model. Plots are shown for $X_{pert} = 0.1, 0.25, 0.3, 0.35$, and 0.4.

FIG. 4. The Lyapunov exponent λ as a function of X_{pert} for various values of the blob radius σ. The point vortex model corresponds to $\sigma = 0.0$.

0.4. In addition, a cat's eye structure begins to form. It is interesting to note that as the subharmonic perturbation approaches 0.5, particles are likely to stay within one periodic window. Complete trapping occurs in the absence of a subharmonic perturbation, i.e., for an unperturbed, steady row of point vortices. In that case, a particle would simply travel along a time-independent streamline within the cat's eye, i.e., its trajectory would be periodic, hence it would never leave the region enclosed by the separatrices. Trapping also occurs in the limit of large perturbations, $X_{pert} \to 0.5$, where macroscopically the flow appears as a row of point vortices of twice the circulation separated by twice the distance as in the unperturbed case. From Fig. 3 we observe that the chaotic regions are most pronounced for weak values of the subharmonic perturbation.

Figure 4 shows a plot of the largest Lyapunov exponent, $\lambda (\lambda = \lim_{t \to \infty} 1/t \{\ln[l(t)]/l(t=0)\})$ for the point vortex model as a function of X_{pert}. The largest Lyapunov exponent can be calculated by tracking the distance l between two particles that are very close to each other initially and letting them evolve in time. Since the distance grows exponentially, it is necessary to renormalize the distance periodically so that a preset threshold is never exceeded. See Refs. [18,19] for a detailed discussion on computations of Lyapunov exponents. The values shown in Fig. 4 are average values taken from several different initial conditions which are then allowed to evolve in time for a duration equal to 80 periods of vortex motion. From the figure, it is clear that for the point vortex model the Lyapunov exponent increases
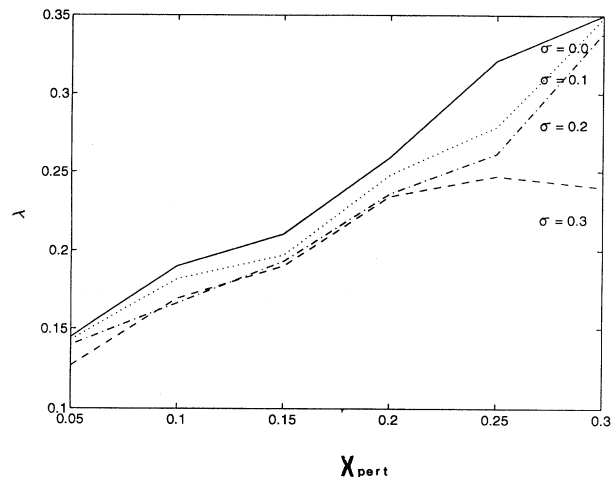
with the size of the perturbation.

We next take a closer look at the implications of the chaotic nature of the flow field on the short-time dynamics. We begin by considering a point vortex row with an intermediate subharmonic strength, with $X_{pert} = 0.3$. This is displayed in Fig. 5, which shows the evolution over one period of a Lagrangian line element initially placed between $(-0.05, 0)$ and the origin, along with the instantaneous streamline pattern. At $t = 0$, the line element is represented by 50 particles. Subsequently, as the line element becomes increasingly stretched, particles are continuously added in order to maintain an adequate resolution, so that after one period the element contains on the order of 20 000 particles. The line element quickly aligns itself with the extensional direction of the local strain field, i.e., with the direction of the streamline along which particles move away from the free stagnation point. This approximate alignment of the line element with the separatrix is a feature observed in all of our simulations. It indicates that the particular initial shape of the tracked line element is of minor importance. However, while the line element experiences continued stretching, the underlying figure eight pattern continues to rotate around the origin, so that the Lagrangian line element never becomes completely aligned with the separatrix. After 0.4 periods $(t = 1.14)$, we obtain a situation in which the line element crosses the separatrix as it loops back to the vicinity of the free stagnation point. Subsequently, this results in a folding event, as some parts of the line element continue to wrap around one vortex, whereas other parts become entrained by the other one. Over the second half period, several more of these folding events occur, along with the continuous stretching. At the end of only one period, each of the two vortices is almost completely surrounded by several segments of the material line element.

In order to demonstrate the influence of the amplitude of the subharmonic component of the flow on the short-time particle motion, we present in Fig. 6 results for the
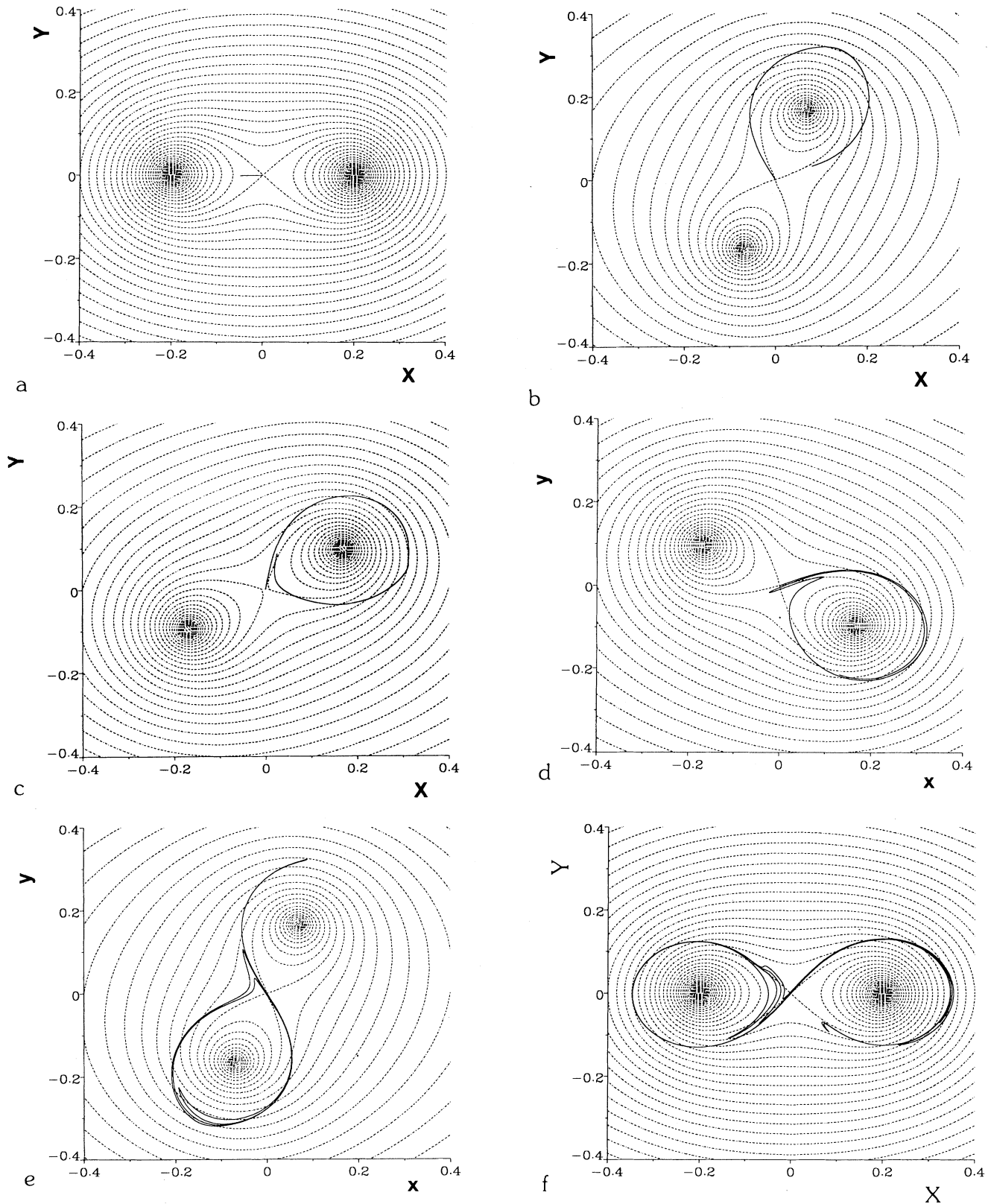
FIG. 5. The evolution over one period of a line element initially located between (−0.05,0) and (0,0), as well as the instantaneous streamline pattern. We observe intense stretching along with several folding events, which are related to the crossing of the separatrix by sections of the line element. $X_{pert} = 0.3$ for $t = 0.0$, 0.85, 1.14, 1.71, 2.28, and 2.85, corresponding to 0, 0.3, 0.4, 0.6, 0.8, and 1.0 periods of the flow.
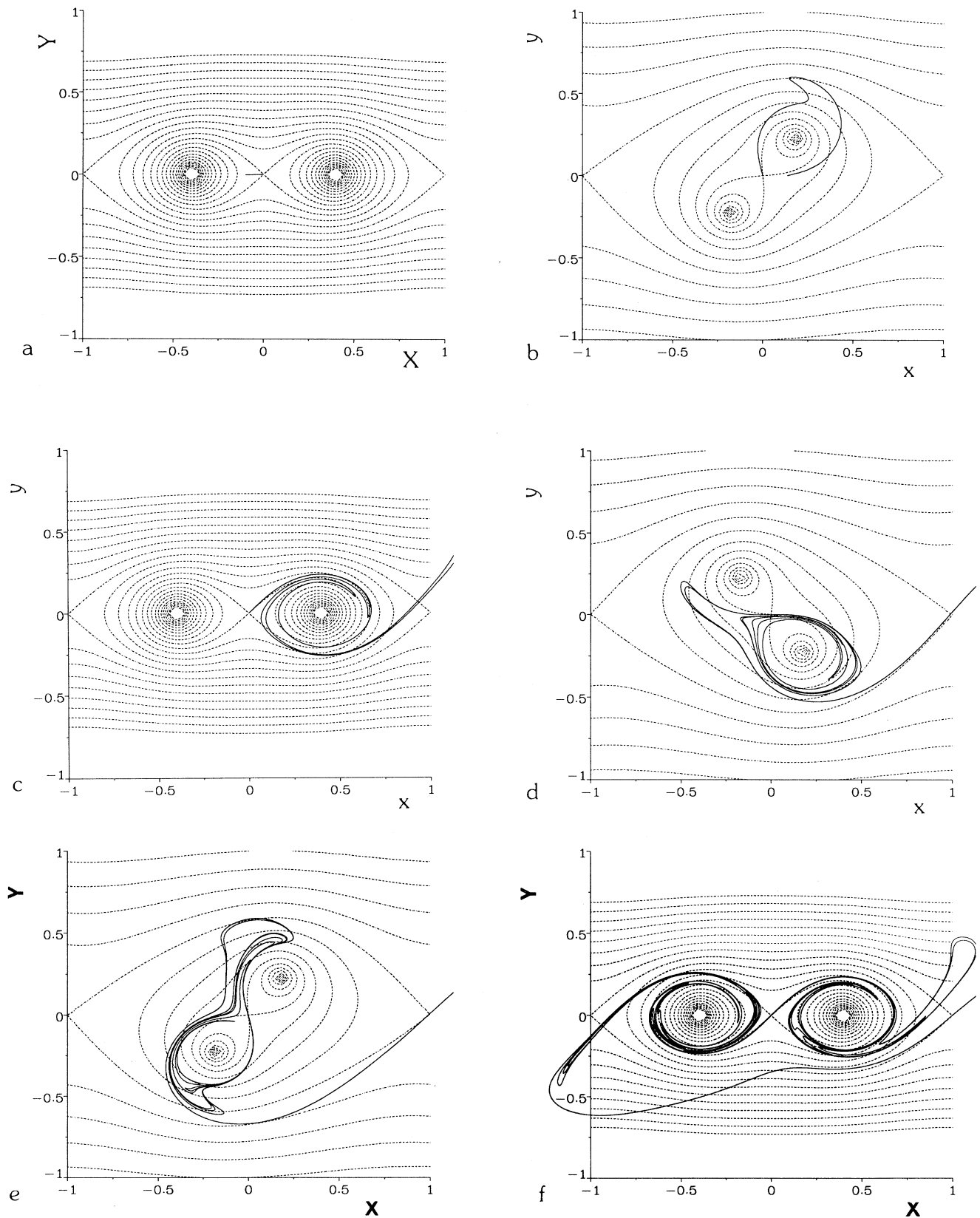
FIG. 6. The evolution of a line element initially located between $(-0.1,0)$ and $(0,0)$ over one period for $X_{pert} = 0.1$. Notice the ejection of some line segments into the free stream and their subsequent reentrainment by neighboring vortex pairs.

evolution of a line element initially placed between $(-0.1,0)$ and $(0,0)$ over one period in a flow with a weaker subharmonic component: X_{pert} is now 0.1. We find that the production of small scales near the origin and generally in the vicinity of the pairing vortices is even more pronounced than in the flow with the larger subharmonic component of Fig. 5. In particular, note that some line segments are ejected into the free stream and convected to neighboring vortex pairs which can then reentrain them. This ejection mechanism had not been observed for the stronger subharmonic perturbation, $X_{\text{pert}} = 0.3$. As will be discussed later, direct Navier-Stokes simulations of pairing demonstrate the formation of spiral arms of spanwise vorticity which are similar in shape to the line element in Fig. 6. The above two simulations indicate that small scales in the deformed line element are not only generated by the ejection of the line element, but also by the intense stretching and folding near the vortex pair. However, especially in view of the findings by Moser and Rogers [13], the ejection of spiral arms of spanwise vorticity play a significant role in the transition process of the mixing layer.

3. Formation of spiral arms and the topology of streamlines

We next investigate this ejection mechanism and the role the subharmonic plays in the ejection in more detail. For this purpose, it is helpful to focus on the streamline pattern in the vicinity of the vortex pair near the origin. Its qualitative evolution is determined by the corotating motion of the nearest two point vortices and the strain field created by all the other vortices in the shear layer. Since we can think of these remaining vortices as a row of vortex pairs about the points $\cdots (-4,0),(-2,0),(2,0),(4,0), \cdots$, the time-averaged strain field created by them near the origin can be approximated by the steady configuration of a row of point vortices of strength 2Γ at the above locations. The velocity field due to this row of vortices from which the central one has been removed is

$$u = (1/2)\frac{\sinh(\pi y)}{\cosh(\pi y)-\cos(\pi x)} - (1/\pi)\frac{y}{x^2+y^2} , \qquad (2.5)$$

$$v = (-1/2)\frac{\sin(\pi x)}{\cosh(\pi y)-\cos(\pi x)} + (1/\pi)\frac{x}{x^2+y^2} . \qquad (2.6)$$

Near the origin, we obtain with $x,y \sim O(\epsilon)$

$$u = (\pi/12)y + O(\epsilon^2) , \qquad (2.7)$$

$$v = (\pi/12)x + O(\epsilon^2) , \qquad (2.8)$$

so that the strain field within which the vortex pair near the origin rotates has the leading-order strength $\pi/12$. To capture the main features of this flow field in as simple a way as possible, we focus on the problem of an isolated pair of corotating point vortices located at (x_{v1},y_{v1}) and $(x_{v2},y_{v2}) = (-x_{v1},-y_{v1})$ in an external strain field that is intended to model the time-averaged effects due to all other rotating vortex pairs. This pure straining motion is represented by the stream function

$$\psi_s(x,y) = (A/2\pi)\{(y^2-x^2)\sin(\alpha)\cos(\alpha)$$
$$+xy[\cos^2(\alpha)-\sin^2(\alpha)]\} , \qquad (2.9)$$

where α controls the direction of the principal axes and A measures the strength of the strain field. For $\alpha = \pi/4$, the direction of the strain field is that seen by the vortices in the infinite row of point vortices. If we render the problem dimensionless in the same way as for the infinite row of point vortices, i.e., by taking the distance l between the unperturbed vortex locations as the characteristic length and the difference in the freestream velocities as the characteristic velocity, we obtain for the dimensionless stream function

$$\psi(x,y) = (1/2\pi)\{\ln[\sqrt{(x-x_{v1})^2+(y-y_{v1})^2}]$$
$$+\ln[\sqrt{(x+x_{v1})^2+(y+y_{v1})^2}]\}$$
$$+S\{(y^2-x^2)\sin(\alpha)\cos(\alpha)$$
$$+xy[\cos^2(\alpha)-\sin^2(\alpha)]\} . \qquad (2.10)$$

Here, $S = (Al^2)/(2\pi\Gamma)$ is the dimensionless parameter denoting the relative strengths of the point vortices and the strain field. An important observation that should be emphasized is that it is useful to study the streamline pattern in a reference frame rotating with the instantaneous angular velocity of the point vortex pair. In this frame, the separatrices no longer rotate. Instead they only perform small oscillations around their time-averaged positions, so that their geometric shape becomes much more helpful for understanding the deformation of fluid elements. Furthermore, in this rotating reference frame, the point vortices remain on the x axis for all times. The stream function in this rotating reference frame becomes

$$\psi(x,y) = (1/2\pi)\left[\ln[\sqrt{(x-x_{v1})^2+y^2}]\right.$$
$$\left. +\ln[\sqrt{(x+x_{v1})^2+y^2}] - \frac{x^2+y^2}{4x_{v1}^2}\right]$$
$$+S\{2y^2\sin(\alpha)\cos(\alpha)$$
$$+xy[\cos^2(\alpha)-\sin^2(\alpha)]\} . \qquad (2.11)$$

Figures 7(a) and 7(b) show the deformation of a line element in a corotating vortex pair under strain $S = \pi/12$ for the different subharmonic perturbations of Figs. 5 and 6, respectively. Also shown are the streamline patterns in the rotating reference frame. The line element deformation shows a striking similarity to Figs. 5 and 6, indicating that the corotating vortex pair under strain approximates the infinite vortex row configuration quite well. In particular, we do not observe an ejection mechanism for the stronger subharmonic perturbation, whereas in the case of the weaker perturbation line segments are ejected into the free stream, in correspondence to the infinite row situation. This different behavior can be understood on the basis of the streamline pattern in the rotating reference frame. For the stronger subharmonic perturbation, the topology of the streamline pattern stays the same over the whole period, i.e., the separatrix continually closes around the individual vortices, so that in the rotat-
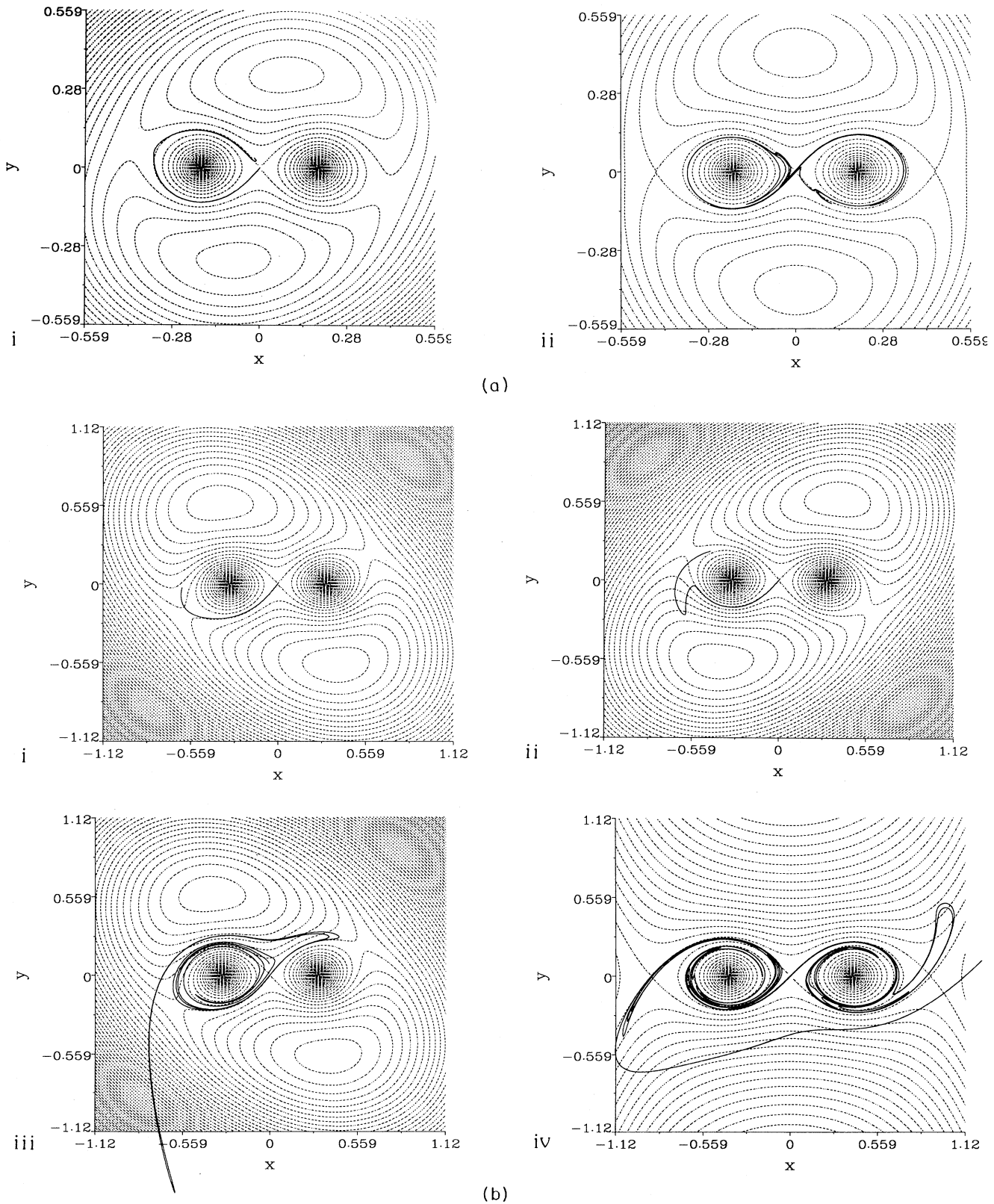
(a)

(b)

FIG. 7. (a) An isolated corotating vortex pair in an external strain field of strength $\pi/12$. Shown are the streamline patterns at times $t = 1.02$ and 2.86 in a reference frame that rotates with the instantaneous angular velocity of the vortices. $X_{\mathrm{pert}} = 0.3$. Notice the similarity of the deformed line element with that in Fig. 5. (b) Same as (a), but with $X_{\mathrm{pert}} = 0.1$ for times $t = 1.9$, 3.34, 7.26, and 8.64. The deformed line element has a strong similarity to that of Fig. 6. Note the topological change in the streamline pattern.
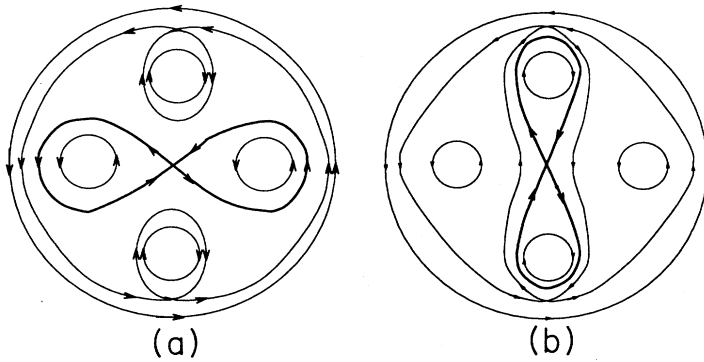
FIG. 8. The qualitative nature of the streamline patterns between which the flow shown in Fig. 7(b) alternates.

ing reference frame the shape of the separatrix remains that of a horizontal figure eight. For the weaker subharmonic perturbation, however, we observe a periodic change in the streamline pattern's topology, where the separatrix changes from a horizontal figure eight to a deformed vertical figure eight. The nature of the streamline patterns for the two different topologies is shown qualitatively in Fig. 8. The instantaneous motion of points along the line element closely follows the separatrices of the streamline pattern shown, and consequently, the changes in the topology lead to successive ejections of line element segments. Note that the above explanation for the formation of spiral arms is purely kinematic. As will be described below, this same topological transition is present both for the vortex blob simulation as well as the direct Navier-Stokes simulation.

While the above results indicate that the subharmonic perturbation is necessary for the generation of small scales by chaotic motion, they also indicate that the smaller amplitude subharmonic leads to a more rapid generation of small scales via the ejection mechanism than the larger amplitude subharmonic. This observation indicates that in an experiment strong forcing of a subharmonic amplitude is not likely to accelerate the production of small scales, in agreement with the experimental observations of several researchers.

B. Vortex blobs

As an intermediate step towards full Navier-Stokes simulations, we next analyze the corresponding situation for vortices with finite support, instead of point vortices. More specifically, we use blobs with a Gaussian distribution in vorticity,

$$\omega = \frac{\Gamma e^{-[r/\sigma]^2}}{\pi \sigma^2} \,, \tag{2.12}$$

where Γ is the vortex strength, r is the distance from the center of the blob, and σ is a characteristic radius of the blob. A review of such two-dimensional vortex methods for flow simulation is provided by Leonard [20]. Because the blobs distribute vorticity in space, the flow field simulated is closer to the Navier-Stokes flow field than that generated by the point vortices. On the other hand, a shortcoming of the vortex blob approximation is that vorticity associated with one vortex blob moves as one entity without any deformation or diffusion. Hence, we can consider the vortex blob model as an intermediate step between the point vortex model and the Navier-Stokes representation.

As in the point vortex model, we start with an infinite row of blobs and give them a subharmonic perturbation to set the vortices in motion. Their motion is due to the induced velocity of the other vortices which can be obtained by approximating all vortices except the nearest one as point vortices (Nakamura, Leonard, and Spalart [21]). The equations of motion then become

$$\dot{x}_{vor} = \frac{-\Gamma}{2} \frac{\sinh(2\pi y_{vor})}{\cosh(2\pi y_{vor}) - \cos(2\pi x_{vor})}$$

$$+ \frac{\Gamma}{2\pi} \frac{y_{vor}}{x_{vor}^2 + y_{vor}^2} e^{-\frac{x_{vor}^2 + y_{vor}^2}{\sigma^2}} \,, \tag{2.13}$$

$$\dot{y}_{vor} = \frac{\Gamma}{2} \frac{\sin(2\pi x_{vor})}{\cosh(2\pi y_{vor}) - \cos(2\pi x_{vor})}$$

$$- \frac{\Gamma}{2\pi} \frac{x_{vor}}{x_{vor}^2 + y_{vor}^2} e^{-\frac{x_{vor}^2 + y_{vor}^2}{\sigma^2}} \,. \tag{2.14}$$

The velocity field can also be obtained by approximating all vortices except the nearest pair as point vortices, hence:

$$\dot{x} = \frac{-\Gamma}{4} \frac{\sinh[\pi(y - y_{vor})]}{\cosh[\pi(y - y_{vor})] - \cos[\pi(x - x_{vor})]} + \frac{\Gamma}{2\pi} \frac{y - y_{vor}}{(x - x_{vor})^2 + (y - y_{vor})^2} e^{-\frac{(x - x_{vor})^2 + (y - y_{vor})^2}{\sigma^2}}$$

$$+ \frac{-\Gamma}{4} \frac{\sinh[\pi(y + y_{vor})]}{\cosh[\pi(y + y_{vor})] - \cos[\pi(x + x_{vor})]} + \frac{\Gamma}{2\pi} \frac{y + y_{vor}}{(x + x_{vor})^2 + (y + y_{vor})^2} e^{-\frac{(x + x_{vor})^2 + (y + y_{vor})^2}{\sigma^2}} \,, \tag{2.15}$$

$$\dot{y} = \frac{\Gamma}{4} \frac{\sin[\pi(x - x_{vor})]}{\cosh[\pi(y - y_{vor})] - \cos[\pi(x - x_{vor})]} - \frac{\Gamma}{2\pi} \frac{x - x_{vor}}{(x - x_{vor})^2 + (y - y_{vor})^2} e^{-\frac{(x - x_{vor})^2 + (y - y_{vor})^2}{\sigma^2}}$$

$$+ \frac{\Gamma}{4} \frac{\sin[\pi(x + x_{vor})]}{\cosh[\pi(y + y_{vor})] - \cos[\pi(x + x_{vor})]} - \frac{\Gamma}{2\pi} \frac{x + x_{vor}}{(x + x_{vor})^2 + (y + y_{vor})^2} e^{-\frac{(x + x_{vor})^2 + (y + y_{vor})^2}{\sigma^2}} . \tag{2.16}$$

The above equations are integrated using a fourth-order Runge-Kutta scheme. Again the periodicity of the vortices is used to reduce the number of computations as described in the section on point vortices.

1. Long-time dynamics

Corresponding to the above investigation of the point vortex model, we now examine the long-term motion of fluid particles through the use of Poincaré sections using vortex blobs. For a vortex core size of $\sigma = 0.1$ and various magnitudes of the subharmonic perturbation, we obtain results very similar to those for point vortices shown in Fig. 3. This indicates that as the vortex core is decreased from 0.1 to zero, the behavior of the point vortex model is recovered in a smooth fashion, as there are no added effects due to the singularity of the point vortices.

By changing the size of the core radius σ, we can now study the effect of varying the vorticity distribution. As the core radius increases to 0.2 (Fig. 9), the size of the islands around the blobs decreases [compare Fig. 9(a), 9(b), and 9(c) with 3(a), 3(b), and 3(c)]. This decrease in the island size is rather counterintuitive: as the vorticity
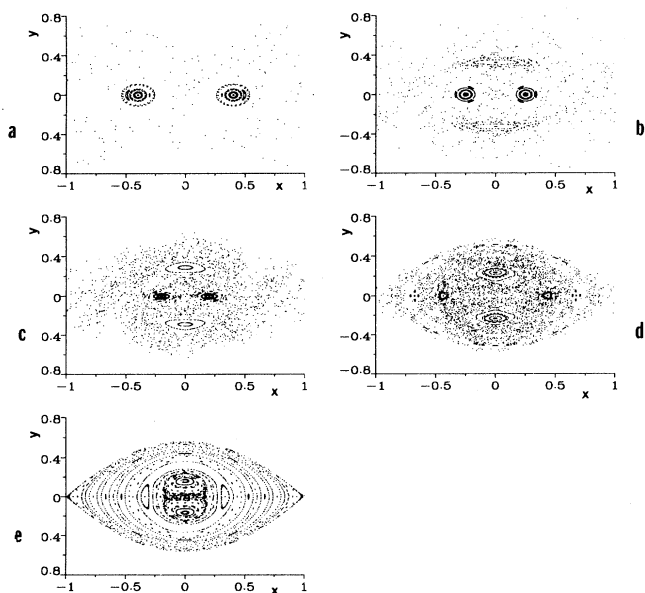

FIG. 9. Poincaré map of particles originally seeded on the x axis and the y axis plotted over a few hundred periods of vortex motion; $\sigma = 0.2$; (a) $X_{pert} = 0.1$, (b) $X_{pert} = 0.25$, (c) $X_{pert} = 0.3$, (d) $X_{pert} = 0.35$, and (e) $X_{pert} = 0.4$. As σ increases, the region of intense chaotic motion increases until the blobs merge, but decreases after the blobs merge.

spreads out more and because the entire vorticity moves as one entity, one expects an increase in the area of the island around the center of the blob. The decrease in the area of the islands continues as we increase the subharmonic perturbation until the blobs merge (i.e., the location of the vorticity maximum shifts to the point midway between the pairing vortices, when $X_{pert} + \sigma = 0.5$). As we continue to increase the subharmonic perturbation, the islands vanish [Fig. 9(d)] and later a new island forms around the center of the merged blobs [Fig. 9(e)], i.e., the originally hyperbolic stagnation point now becomes elliptic. Similar trends are observed using vortex blobs with larger core radii. In short, as the core radius increases, the area of the chaotic region and, hence, mixing increases until vortex merger but shrinks beyond the merger.

In order to quantify the intensity of mixing, we use the Lyapunov exponent, the estimation of which was outlined in the section on point vortices, cf. Fig. 4. The largest exponent is positive in the chaotic regions and it increases as X_{pert} is increased. This indicates that the intensity of the mixing increases even though the mixing is localized. As the blobs move closer to each other (or as X_{pert} is increased) the velocity gradients and the unsteadiness are intensified in the region midway between the vortices leading to high strain, which in turn leads to the extensive stretching. However, if the vortices merge (i.e., $X_{pert} + \sigma > 0.5$), the fixed point at the center changes in nature from hyperbolic to elliptic, thereby modifying the strain field. As a result, if X_{pert} is increased further, the unsteadiness decreases, leading to a reduction in the Lyapunov exponent. Also, the intensity of mixing increases as the radius of the blob decreases. Therefore, mixing of fluid particles in the present model is a compromise between the region of mixing and its intensity.

2. Short-time dynamics and streamline topology

As for the point vortex model, we next examine some aspects of short-time mixing by tracking a small line element seeded near the origin. For vortex blobs of core radii $\sigma = 0.1$ with two different levels of subharmonic perturbations, $X_{pert} = 0.1$ an 0.3, we find that after equal times, the stretching and folding is more intense for the case with the larger subharmonic perturbation. We can determine a quantitative measure of the stretching by using a stretching parameter s defined by

$$s = \frac{1}{T} \ln \left[\frac{L}{L_0} \right] .$$

This stretching parameter increases with the magnitude of the subharmonic perturbation. However, this trend is reversed if we make our observations after an equal number of periods rather than at equal times. An equal number of periods corresponds to a larger time for the smaller subharmonic perturbations due to the smaller induced velocity at the vortex centers. The stretching parameter can be redefined using the number of periods instead of time as follows:

$$s' = \frac{1}{N}\ln\left[\frac{L}{L_0}\right] ,$$

where N denotes the number of periods. This form of the stretching parameter decreases with increasing subharmonic amplitude, so that after the same number of periods the flow with the smallest subharmonic perturbation produces the largest amount of stretching and folding (Fig. 10).

The increase in intensity of mixing on a per period basis is related to the topological transition described earlier for the point vortex model. We observe this topological change by again plotting the stream function in a coordinate frame that moves with the pairing vortices. Figure 11 displays the stream function for various times up to a quarter of the period for the smaller subharmonic perturbation. As previously observed for the point vortex model, we see that the topology of the stagnation point streamline changes from a horizontal to a vertical figure eight pattern and back in one quarter of a period. By virtue of the reflectional symmetries about the x and y axes, similar streamline patterns are seen for successive quarters of the period. When the topology changes to a vertical figure eight, line elements can be ejected, and as a result can undergo more intense stretching and folding per period. This intensification of stretching and folding, in turn, produces more small scales per period. On the other hand, for the stronger subharmonic perturbation
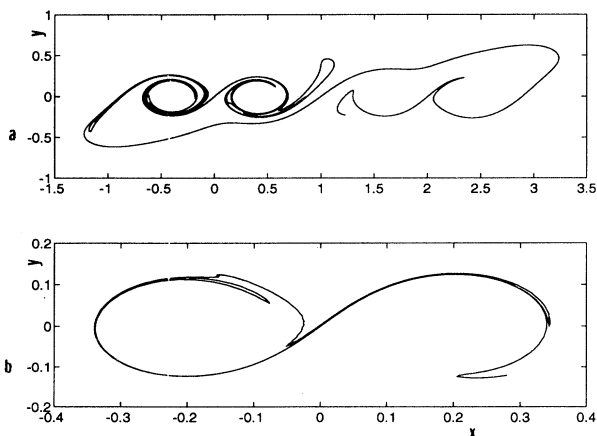

FIG. 10. Stretching of a line element at the end of one period when $\sigma = 0.1$; (a) $X_{\text{pert}} = 0.1$ and (b) $X_{\text{pert}} = 0.3$. Notice that after one period the smallest subharmonic perturbation produces the largest stretching and folding, which appears to be related to the topological transition seen in the streamline topology (Fig. 8).
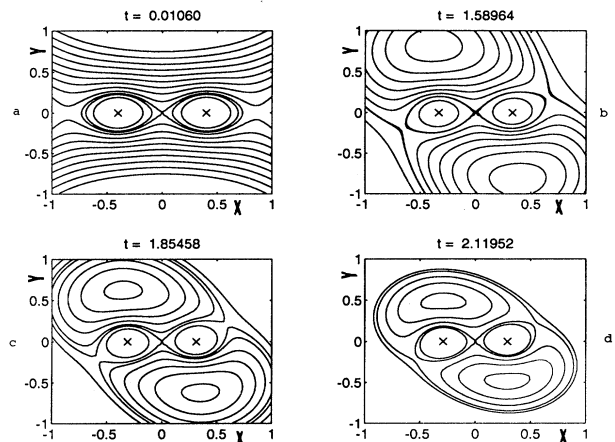

FIG. 11. Streamline pattern in a coordinate frame that moves with the vortices; $X_{\text{pert}} = 0.1$, $\sigma = 0.1$; (a) $t = 0.0106$, (b) $t = 1.5896$, (c) $t = 1.8546$, and (d) $t = 2.1195$. Notice that the topology changes from a horizontal ∞ pattern to a vertical 8 pattern and back to the horizontal ∞ pattern.

no such topological transition occurs and hence the line element remains confined to a more limited region.

III. NAVIER-STOKES CALCULATION

In order to assess the extent to which the behavior observed for the point vortex and the vortex blob models is reproduced in a viscously evolving mixing layer, we have conducted a set of full Navier-Stokes simulations. For comparison purposes, we track passive line elements in Navier-Stokes flow fields characterized by different values of fundamental and subharmonic perturbation amplitudes, a_f and a_s. We use a pseudospectral simulation to generate the flow fields in this section, which is a modified version of the stratified shear-layer code of Wang and Maxey [22]. The initial flow field consists of a tanh velocity profile of the horizontal velocity component as a base flow along with perturbations. These perturbations are given by the eigenfunction corresponding to the most unstable wave number from inviscid theory [23] along with the same form of perturbation applied to the subharmonic wave number. The phase of the subharmonic perturbation was selected such that it results in a vortex pairing event, rather than in vortex tearing.

The simulation solves the rotational form of the incompressible Navier-Stokes equations in two dimensions:

$$u_{ix_i} = 0 , \tag{3.1}$$

$$u_{it} + (\omega \times u)_i = -P_{x_i} + \frac{1}{\text{Re}}u_{ix_jx_j} , \tag{3.2}$$

where for our two-dimensional flow $i = 1, 3$. Here, u denotes the velocity, P denotes the pressure, ω denotes the velocity, and Re indicates the Reynolds number. We solve these equations for the case of a temporal shear layer, using periodic boundary conditions in the horizontal direction. Thus, in order to satisfy the boundary conditions in both directions we expand the velocity field in

terms of its Fourier coefficients $\hat{u}_\alpha$ as

$$u_\alpha(x_1,x_3,t)=\sum_{k_1}\sum_{k_3}\hat{u}_\alpha(k_1,k_3,t)\exp(ik_1x_1)$$

$$\times\begin{cases}\cos(k_3x_3)\,, & \alpha=1\\\sin(k_1x_1)\,, & \alpha=3\,,\end{cases} \quad (3.3)$$

where k_i are the wave number vectors. We advance the momentum equation in time using a second-order Adams-Bashforth scheme on the nonlinear terms and a second-order Crank-Nicolson scheme on the linear terms. The continuity equation and pressure terms are satisfied by applying the following filter to the Fourier coefficients after the time advancement:

$$\hat{u}_i=\left[\delta_{ij}-\frac{k_ik_j}{k^2}\right]\hat{u}_j\,.$$

In addition to solving for the flow field, we must also solve for the time evolution of the particle positions, i.e., we need to integrate the velocities $(dx_i/dt=u_i)$. The issue here is how to interpolate the velocity field at the particle positions. We use the Hermite interpolation scheme of Balachandar and Maxey [24], which takes advantage of the spectral accuracy used in calculating the velocity derivatives. We then apply a fourth-order Adams-Bashforth method to advance the particle locations.

We should mention at this point the differences between the perturbations used to initialize the instabilities in the Navier-Stokes simulation and the previous models. For the Navier-Stokes simulation, we require both basic and subharmonic perturbations, whereas in the point vortex and vortex blob models we introduce a subharmonic perturbation by displacing vortex pairs (changing the pairing distance). The basic perturbations for these models are the vortices themselves. In addition to this difference in basic perturbations between the Navier-Stokes simulation and models, the subharmonic perturbations also differ. In the point vortex and vortex blob models, changes to the subharmonic perturbation modify only the pairing distance. In the Navier-Stokes calculation, however, changing the subharmonic perturbation results in modifications to not only the pairing distance but also the effective core radius of the vortices. In the vortex blob model the core radius is an independent parameter, and thus can be controlled separately from the pairing distance. The fact that the subharmonic perturbation in the Navier-Stokes flow affects both pairing distance and the effective core radius reflects the ability of the vortices in the flow to be diffused and distorted. This effect is absent in the models, where the vortices are convected without change to their strength or structure. To avoid any confusion about what we mean by subharmonic perturbation, from this point on we refer to the perturbation applied to the vortex models as changes to the pairing distance, and reserve the term subharmonic perturbation to mean the classical perturbation used in the Navier-Stokes simulations.

Because the subharmonic perturbation applied to the Navier-Stokes simulation affects the flow in more ways than mere modification of the pairing distance, we first

must address how changes in the subharmonic perturbations relate to the core radius and pairing distance in preceding sections. After this "mapping" has been established, we can then proceed to analyzing how well the mechanisms for mixing found in the model flows apply to the Navier-Stokes flow. To aid us in this goal, we examine the vorticity contours for simulations with different values of basic and subharmonic perturbations in Figs. 12–15. The different levels of vorticity contours have values $10,20,30\cdots90\%$ of the maximum vorticity. The two innermost contours, corresponding to the 90% level, encompass the two vortex centers (i.e., the locations of maximum vorticity). The number of isocontours present between the two vortex centers gives an indication of the core radius, provided the vortex centers are approximately the same distance apart: as this number increases, the core radius decreases. We take as a reference case Fig. 12, in which both the fundamental and the subharmonic perturbation amplitudes have a value of 0.01 and then we consider the effect of varying both these amplitudes one
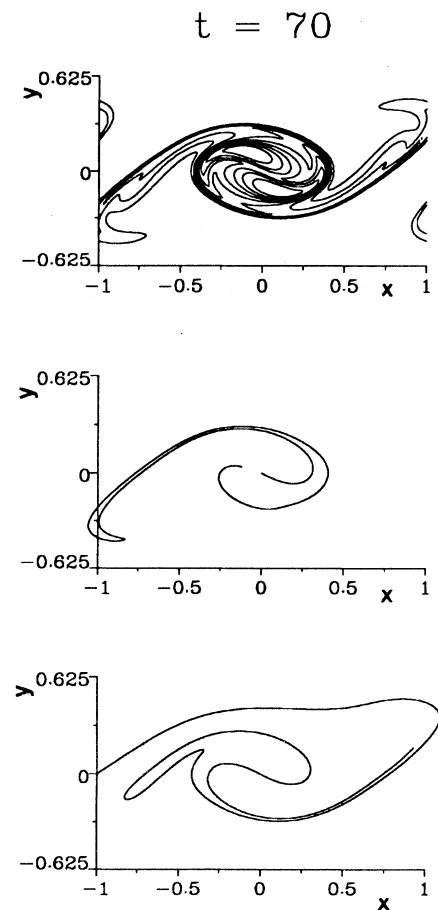

FIG. 12. Vorticity contours and two line elements (one located at the stagnation point between the pairing vortices and the other located at the stagnation point between vortex pairs) for a 2D Navier-Stokes flow plotted for $t=70$; $a_f=0.01$ and $a_s=0.01$. This equal amplitude simulation serves as the reference with which the other simulations are compared.

at a time. In the reference case, there are three isocontours between the two vorticity maxima. This number increases to four if the subharmonic perturbation (a_s) is decreased (while maintaining the same basic perturbation amplitude), indicating that the core size decreases with a_s (Fig. 13). Conversely, when a_s is increased to 0.02, the core radius increases, which can be inferred from the fact that the number of isocontours between the two vortices has decreased to two (Fig. 14). Even more pronounced is the increase in core radius if the basic perturbation is decreased to 0.002, because there is only one isocontour between the pairing vortices (Fig. 15). In addition, the variations in the core size with respect to variations in the perturbation amplitudes can be seen visually, too, by superimposing the contour plots.

However, it is difficult to visualize the variations in the pairing distance using the vorticity contours. To study these variations, we plot the time series of the vertical location of the center of a pairing vortex (Fig. 16). From these plots the rate of rotation (of the vortex center about

the origin) can be determined. The rate of rotation increases if the pairing distance decreases. Therefore, from the rotation rates that can be estimated using Figs. 16(a), 16(b), and 16(c), it is clear that the average pairing distance (averaged over $t=0-75$) increases when a_s is decreased, and vice versa. Similarly, a decrease in the pairing distance is observed if the basic perturbation is decreased [Fig. 16(d)]. In summary, the effect of increasing the subharmonic perturbation is to increase the core radius σ, but to decrease the pairing distance. Further, the same trends in the pairing distance and the core radius can be observed if the basic amplitude is decreased.

Having established a connection between the effects of the basic and the subharmonic perturbations in the Navier-Stokes simulations and the displacement perturbations X_{pert} and core radius σ in the vortex blob model, we can now proceed to examine the mixing processes in these cases. We do this by tracking two material line segments in the Navier-Stokes flow. The first line element extends from $x=0$ to $x=0.05$, while the second line ele-
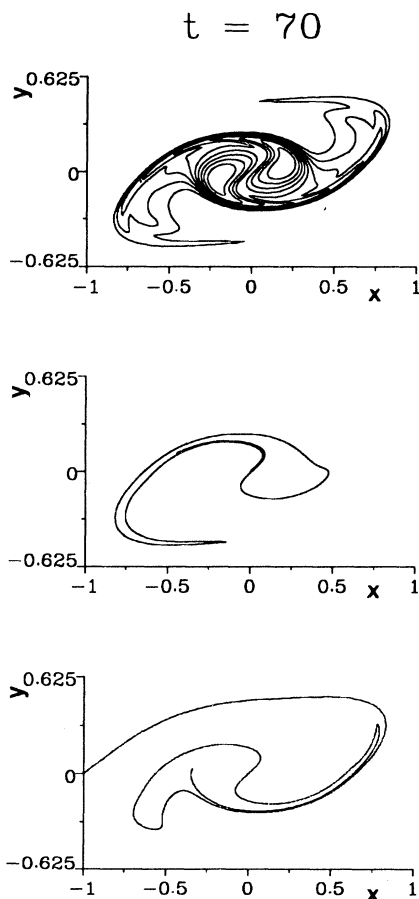

FIG. 13. Vorticity contours and two line elements (one located at the stagnation point between the pairing vortices and the other located at the stagnation point between vortex pairs) for a 2D Navier-Stokes flow plotted for $t=70$; $a_f=0.01$ and $a_s=0.005$. Decreasing the subharmonic amplitude decreases both X_{pert} and σ. The overall effect of the decreased X_{pert} and the decreased σ is to increase the stretching.
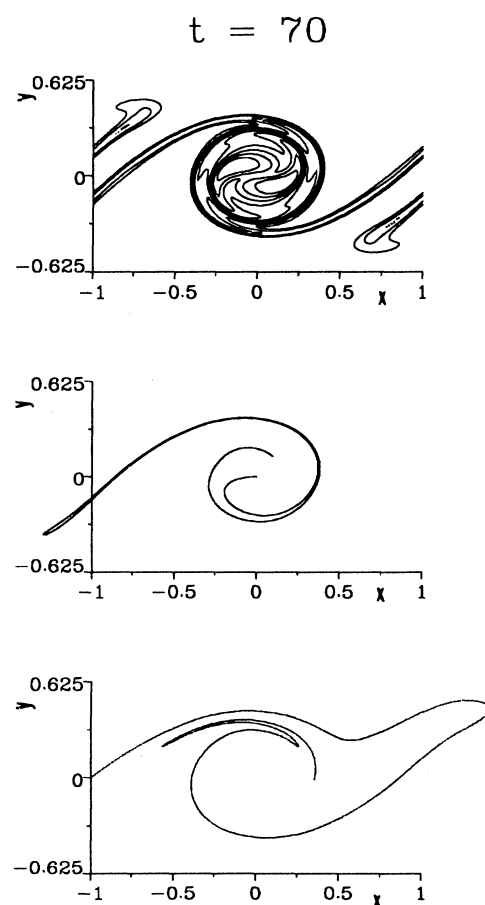
FIG. 14. Vorticity contours and two line elements (one located at the stagnation point between the pairing vortices and the other located at the stagnation point between vortex pairs) for a 2D Navier-Stokes flow plotted for $t=70$; $a_f=0.01$ and $a_s=0.02$. Increasing the subharmonic amplitude increases both X_{pert} and σ. The overall effect of the increased X_{pert} and the increased σ is to increase the stretching marginally.

ment extends from $x = -1.0$ to -0.95 when $t = 0$, and both are displayed in Figs. 12–15. We first address the stretching of material lines. Recall that in the vortex blob model the stretching parameter based on time s increases as both the pairing distance and core radius decreases. In the Navier-Stokes flow, as a_s is decreased to 0.005, the core radius decreases but the pairing distance increases. Thus we have two competing phenomena as far as the stretching is concerned. The more dominant effect, in this case, is the change in the core radius, since we observe an increase in stretching of the line elements (compare Fig. 13 with Fig. 12). Further, the number of folds also increase. When a_s is increased to 0.02, the core radius increases but the pairing distance decreases. These changes in core radius and pairing distance produce a marginal increase in the stretching (Fig. 14).
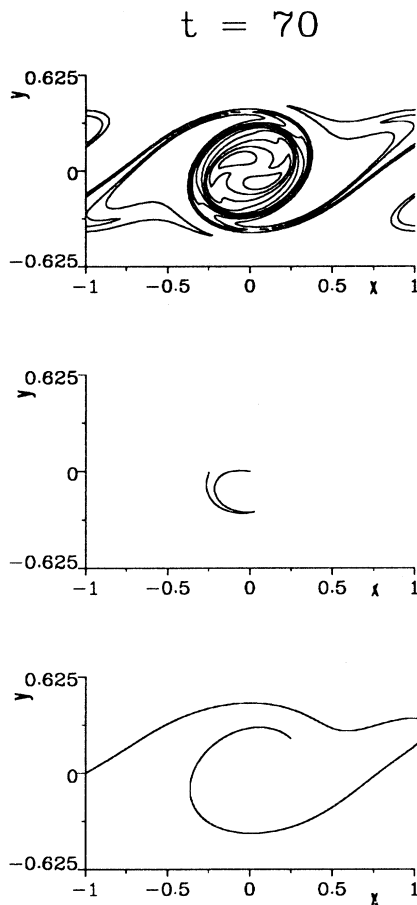

FIG. 15. Vorticity contours and two line elements (one located at the stagnation point between the pairing vortices and the other located at the stagnation point between vortex pairs) for a 2D Navier-Stokes flow plotted for $t = 70$; $a_f = 0.002$ and $a_s = 0.01$. Decreasing the basic amplitude increases both X_{pert} and σ. The overall effect of the increased X_{pert} and the increased σ is to decrease the stretching. This combination of a_f and a_s corresponds to the largest X_{pert} which, in turn, causes the line element to remain trapped without any ejection. This is in agreement with results from the point vortex model and the blob model.
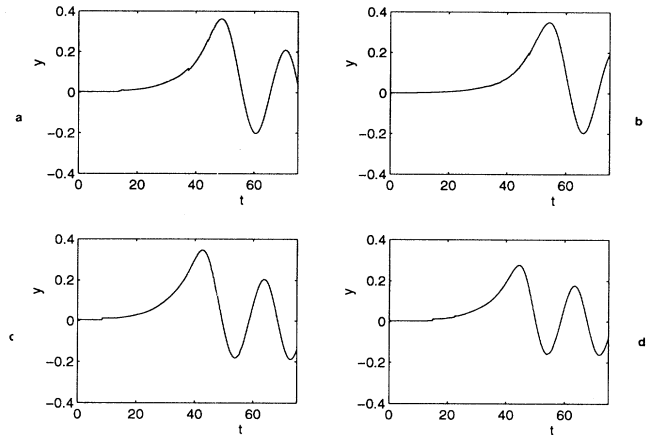

FIG. 16. The y ordinate of the location of vorticity maximum plotted as a function of time. The higher the frequency, the larger the X_{pert}. (a) $a_f = 0.01$, $a_s = 0.01$; (b) $a_f = 0.01$, $a_s = 0.005$; (c) $a_f = 0.01$, $a_s = 0.02$; (d) $a_f = 0.002$ $a_s = 0.01$. (d) corresponds to the largest X_{pert}, which leads to the suppression of ejection (Fig. 15).

Next we consider the effect of varying the basic amplitude on the stretching. If the basic perturbation is decreased, the stretching decreases, again due to the increased σ (Fig. 15). Further, the line element does not get ejected in this case because the value of X_{pert} is high. This lack of ejection is very similar to those observed in
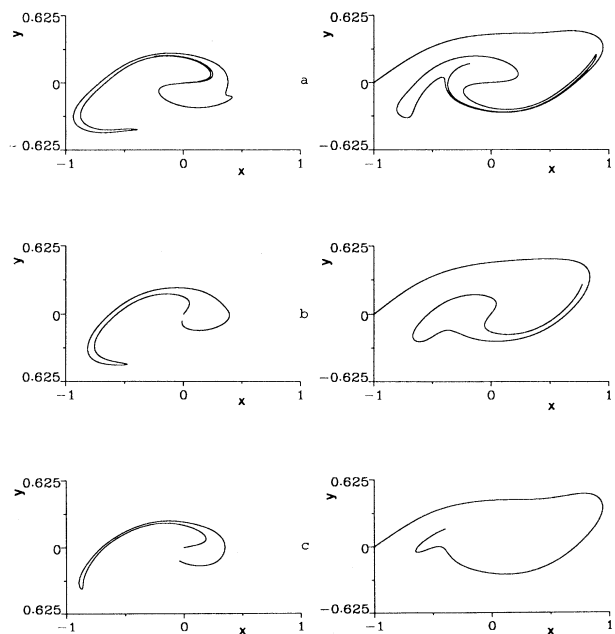

FIG. 17. Two line elements (one located at the stagnation point between the pairing vortices and the other located at the stagnation point between vortex pairs) plotted at the end of one period; $a_f = 0.01$; (a) $a_s = 0.005$, (b) $a_s = 0.01$, and (c) $a_s = 0.02$. The lowest subharmonic amplitude case gives the smallest X_{pert} which, in turn, causes the maximum stretching at the end of one period (compare with Fig. 10).
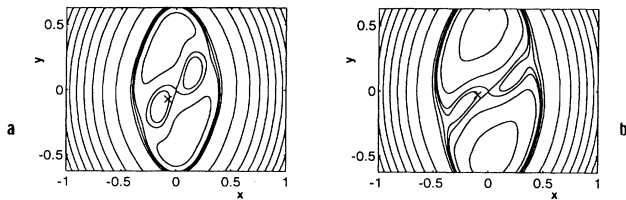
FIG. 18. Streamline pattern plotted in a coordinate frame that moves with the vortices; $a_f = 0.01$ and $a_s = 0.005$; (a) $t = 58$ and (b) $t = 60$. Notice that this combination of amplitudes corresponds to the lowest X_{pert} in the blob simulation and, consequently, with this combination of amplitudes we see a topological transition while for other combinations we do not (compare with Fig. 11).

the point vortex model and the blob model. Conversely, if the basic perturbation is increased to 0.05, the stretching increases because the core radius decreases. The line elements for this case are very similar to those in Fig. 13 and hence not plotted. Overall, the behavior of stretching in the Navier-Stokes flow agrees well with that in the vortex blob model.

So far we have considered stretching in terms of the time. We now discuss the stretching parameter s' on a per period basis. In the blob simulations, after the same number of periods, the stretching increased as the pairing distance increased while maintaining a constant core radius. Similar results can be seen in the Navier-Stokes calculations, although σ cannot be held constant. Figure 17 shows the deformed line elements at the end of one period for different values of the subharmonic perturbation. As the amplitude of the subharmonic perturbation decreases, the pairing distance increases and the flow with the largest pairing distance (i.e., flow with lowest subharmonic amplitude) shows the maximum stretching [Fig. 17(a)]. As in the previous two models, the stagnation point streamline of the flow with the largest pairing distance plotted in a coordinate frame that moves with the vorticity maximum shows a topological transition. The separatrix changes from a horizontal to a vertical figure eight, which enhances the stretching and folding of the line element per period (Fig. 18). This should be compared with Figs. 8 and 11. As a result, the flow that exhibits such a topological transition produces the maximum small scales per period. Navier-Stokes flows with a smaller pairing distance do not show such a topological transition, which leads to decreased stretching of the line element per period, and this result is similar to that in the point vortex model and the blob model. Further, the largest X_{pert} case (Fig. 15) does not exhibit any line element ejection, which is also similar to the largest X_{pert} cases in both the point vortex model and the blob model.

IV. DISCUSSION

We now attempt to make a connection with experimental and computational mixing layer observations of other authors. For this purpose, two different approaches are possible. In the first one, we can compare the evolving shapes of the above line elements with the

shapes of two-dimensional scalar interfaces or spanwise vorticity contours in order to search for similarities. This is based primarily on the fact that the unstable manifolds in some sense act as attractors, and hence scalar interfaces or vorticity contours should somehow reflect their shape. See Beigie, Leonard, and Wiggins [16] and Rom-Keddar, Leonard, and Wiggins [17] for more details on this. In particular, Beigie, Leonard, and Wiggins describe in detail the stretching and diffusion in a class of chaotic tangles associated with fluids described by periodically forced two-dimensional dynamical systems. Their study focuses on the material curve that lies initially on the unstable manifold segment of the boundary of what they call the "entraining turnstile" lobe. However, since they limit themselves to small amplitude perturbations, they do not observe the topological transition of the streamline pattern that represents one of the main findings of our study. In the second approach, we interpret the above line elements as projections in the spanwise direction of wavy three-dimensional lines, and we can then look for similarities between the evolution of these lines and the stretching and amplification of weak streamwise braid vorticity in plane mixing layers. As mentioned in the introduction, this concept of analyzing the deformation of passive line elements in a simple two-dimensional flow field in order to draw conclusions about the evolution of initially weak streamwise vorticity is similar in spirit to the scenario developed by Bernal and Roshko [9] to explain the formation of counterrotating streamwise vortex structures in the braid region between the Kelvin-Helmholtz rollers. They inferred the large amplitude three-dimensional deformation of an initially slightly perturbed spanwise vortex line near the free stagnation point in the braid region on the basis of the two-dimensional deformation field of a frozen point vortex array. We merely attempt to extend their concept from a steady flow field to one that evolves in time as a result of an additional subharmonic disturbance.

We begin by comparing the two-dimensional observations of other authors. Koochesfahani and Dimotakis [15], in their study of mixing layer transition, visualize the scalar field. In their figure 7(a), lobes can be seen to evolve in between vortices proceeding toward a pairing that resemble the ones of Figs. 12–15. We further note the similarity between these lobes and those observed by Meiburg and Newton [25] in a mixing layer in a different context. In addition, the visualization by Koochesfahani and Dimotakis of pairing vortices [their figure 7(b)] shows these to be surrounded by narrow filaments of fluid coming from both streams, resembling our Fig. 6(f). Moser and Roger's [13] computation of a scalar field at $Sc = 1$ in a pretransitional mixing layer undergoing the second pairing (their figure 30) shows a similar lobe formation and beginning filamentation of the isoconcentration lines near the surviving braid stagnation point. This is an indication that a stretching and folding mechanism similar to the one discussed above is present and can subsequently affect the formation of small scales. It is interesting to note that their picture was taken during the second pairing, thereby giving the stretching and folding mechanism in between pairs enough time to evolve to

large amplitudes. As far as the spanwise vorticity field is concerned, several authors (Martel, Mora, and Jimenez [14], Moser and Rogers [13]) report the formation of spiral arms of vorticity during a pairing event. For example, the arms visible in figures 1(a) and 1(b) of Moser and Rogers [13] resemble some of the folds visible in our

Fig. 6, again suggesting a kinematic relationship.

As far as the second interpretation given above is concerned, namely, in terms of stretched streamwise vorticity, Fig. 19 shows the deformation of a three-dimensional passive line initially perturbed sinusoidally in the spanwise direction. By interpreting this line as a vortex line,
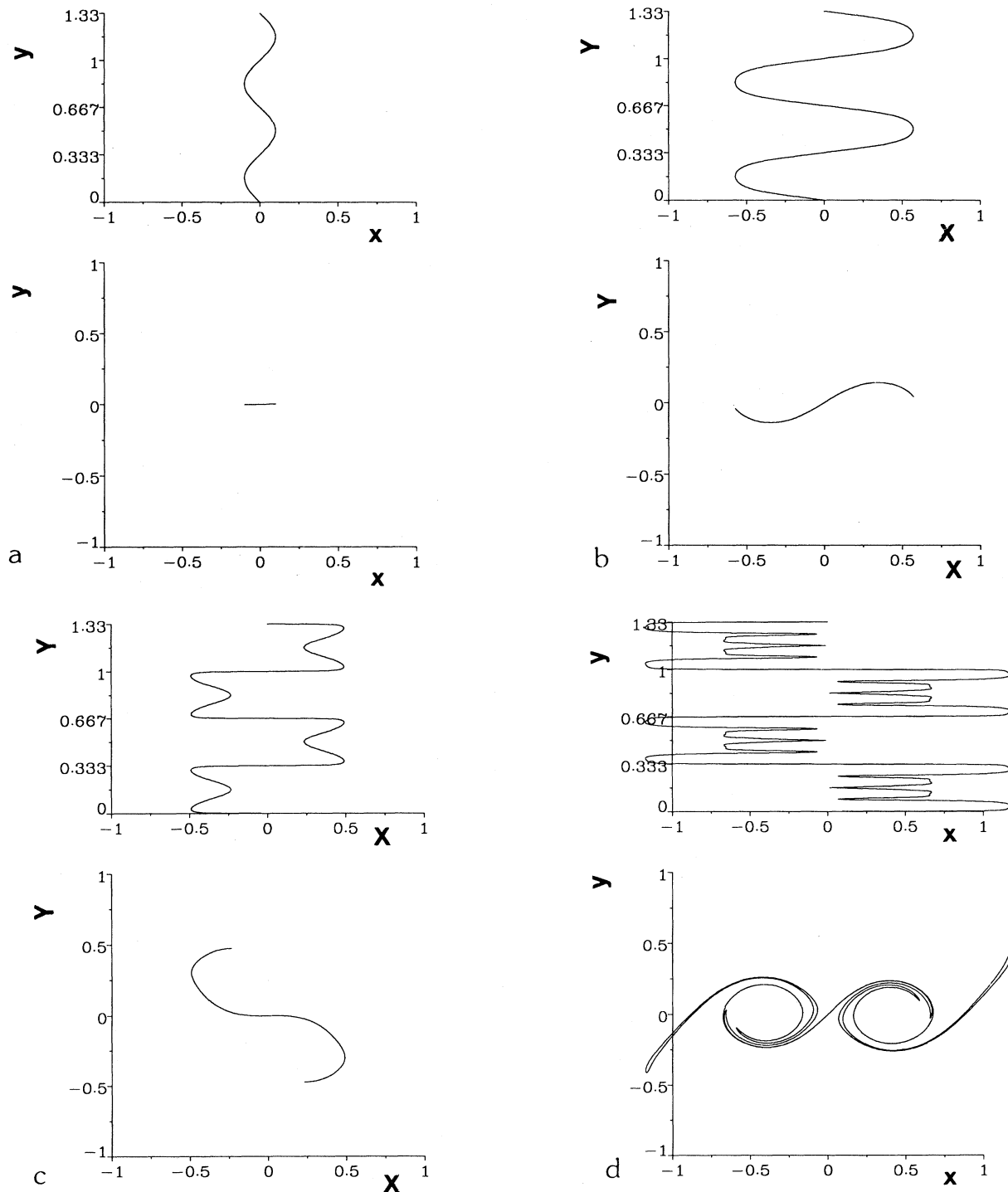
FIG. 19. Interpretation of stretched line element initially located between ($-0.1,0$) and ($0.1,0$) for $X_{\mathrm{pert}}=0.1$ as a three-dimensional passive line initially perturbed sinusoidally in the spanwise direction. Shown are side and top views for (a) 0, (b) 0.1, (c) 0.2, (d) 0.5 periods.

we find that over one period a streamwise vortex can wrap around a spanwise roller several times. In this way, a new mechanism for the generation of strong streamwise vorticity seems possible: streamwise vorticity amplification by multiple wrapping. Furthermore, one can speculate that a configuration in which streamwise vortex tubes wrap around the Kelvin-Helmholtz rollers more than once might allow for additional instability modes such as a Widnall type vortex ring instability or Crow type instability of neighboring vortex tubes. Mechanisms such as these can then further accelerate the small scale production.

For a preliminary qualitative comparison as far as streamwise vorticity deformation is concerned, we can again refer to the results of Moser and Rogers [13]. Stretching and folding near the pairing vortices is detectable in the streamwise vorticity contours of their calculation concerning the growth of infinitesimal three-dimensional perturbations, i.e., in their figure 8, which again shows similarities with our Fig. 6. This folding becomes more pronounced with every successive pairing event as the local Reynolds number increases and the relative importance of viscous diffusion decreases, thereby rendering smaller scales visible. The authors themselves refer to the "folding over" of the streamwise perturbation vorticity "resulting in striated disturbances." In addition, the streamwise vortex lines they show for the engulfed braids after one pairing in a fully nonlinear transitional calculation (their figure 18) have already completely wrapped around the pairing vortices in a fashion similar to the passive lines in our Fig. 19. It should be pointed out that if these mechanisms become visible already at the relatively low Reynolds numbers accessible by direct numerical simulation, they can be expected to play an even more pronounced role at the often higher experimental Reynolds numbers.

Finally, it should be emphasized that the small scale production mechanisms identified and described here do not exclude or replace those postulated by other investigations, such as the secondary rollups of emerging thin shear layers seen by Moser and Rogers [13] or the secondary instability of high shear regions observed by Nygaard and Glezer [26]. The processes discussed here, rather, serve to amplify such two- and three-dimensional inhomogeneities and accelerate their breakdown to smaller scales.

ACKNOWLEDGMENTS

APPENDIX

Particle dynamics in the quasiperiodic region

We analyze the motion of a particle that starts a distance L from the left vortex along the horizontal line connecting the two vortices a distance D apart, as shown in Fig. 1. If we imagine that each pair of rotating vortices is isolated from the effects of other rotating pairs, then the vortex motion will be circular with characteristic frequency ω_c given by

$$\omega_c = \Gamma / (2\pi^2 D^2) \ . \tag{A1}$$

For our model of an infinite row of point vortices, this result is asymptotically valid in the limit of very dominant subharmonic motion ($D \rightarrow 0$ or, equivalently, $X_{\text{pert}} \rightarrow 0.5$). In a similar way, the frequency ω of a particle that starts a small distance L from the vortex center is given by

$$\omega = \Gamma / (4\pi^2 L^2) \ . \tag{A2}$$

Again, this result is asymptotically correct in the limit as the particle position approaches the location of the point vortex, ($L \rightarrow 0, L/D \ll 1$). If we consider a particle initially close to a point vortex in a flow with a strong
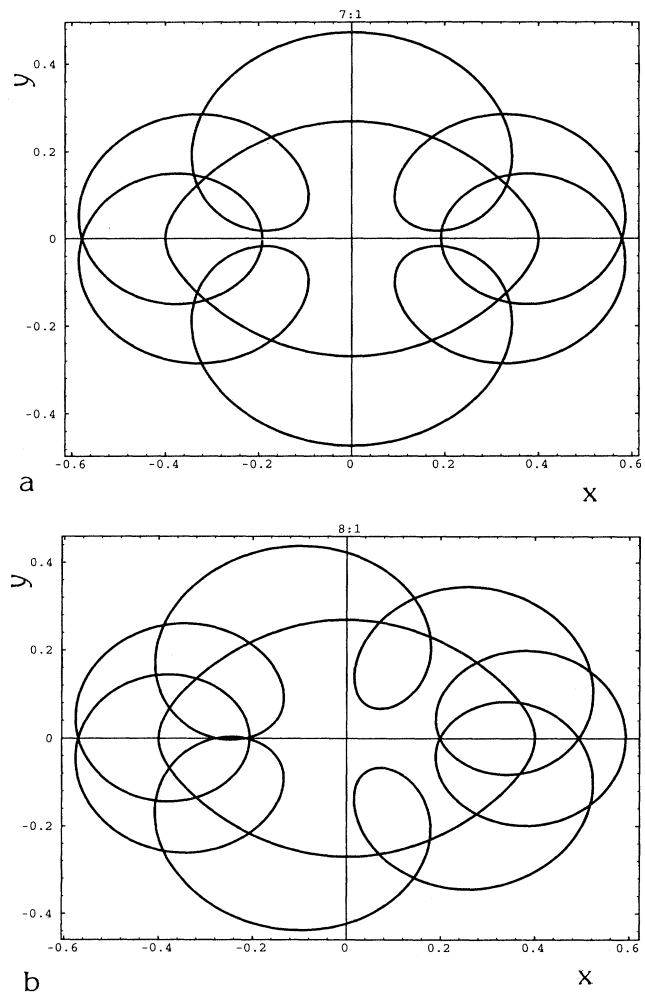

FIG. 20. Periodic orbits for $D = 0.8$, i.e., $X_{\text{pert}} = 0.1$. (a) $n = 7$; note the reflectional symmetry across both axes; (b) $n = 8$; note the reflectional symmetry across only the x axis.
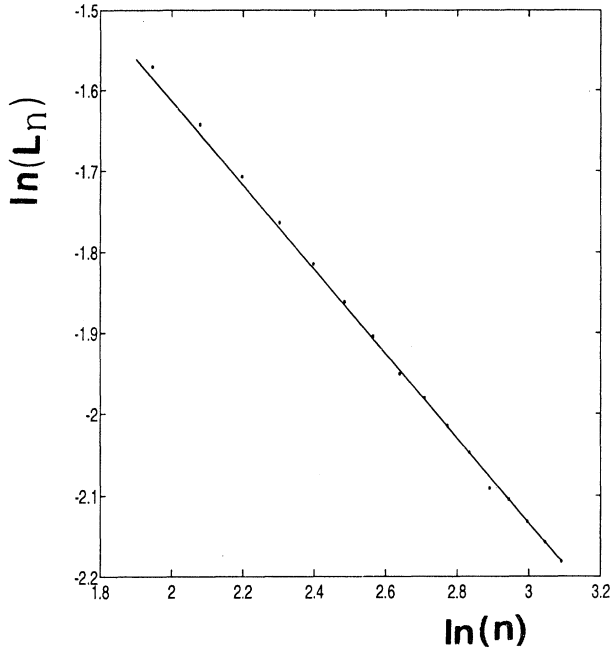
FIG. 21. L_n vs n plotted on a log-log scale. This figure shows power law behavior $L_n \sim n^{-\alpha}$, with $\alpha = 0.521\,281$.
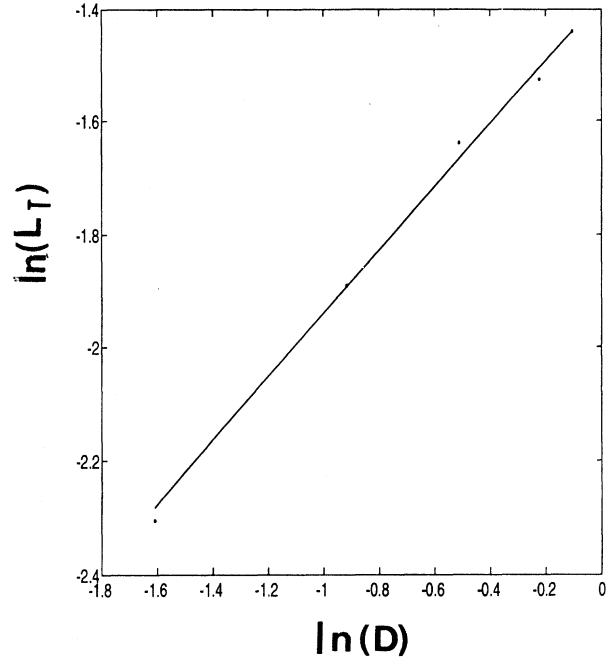

FIG. 22. L_T vs D plotted on a log-log scale. This figure shows power law form $L_T \sim D^\beta$, where $\beta = 0.569\,894$.

subharmonic component, then we can approximate the value of L that results in a frequency ratio $\omega/\omega_c = n$, where n is an integer, as

$$L_n \approx D/\sqrt{2n} \ . \tag{A3}$$

Figures 20(a) and 20(b) show the particle orbits corresponding to $n = 7$ and $n = 8$ for $D = 0.8$. Since the initial particle locations are on the horizontal axis, all orbits corresponding to odd n have reflectional symmetry across both the x and y axes, while all orbits corresponding to even n have reflectional symmetry across only the x axis. Of course, between any two periodic orbits corresponding to consecutive values of n lies a dense family of quasi-periodic orbits whose frequency ratios are irrational, as well as dense family of periodic orbits with higher frequency ratios, n/m, where n is the integer number of times a particle circles the vortex, and m is the integer number of times the vortices circle each other.

The values of L_n versus n, which were evaluated numerically by means of a Newton iteration procedure, are

TABLE I. Comparison of values predicted using $\alpha = 0.5$ and $0.521\,281$ with numerically computed "exact" values for L_{15} through L_{20}.

	Predicted with $\alpha = 0.5$	Predicted with $\alpha = 0.521\,281$	Exact
L_{15}	0.137\,977	0.137\,985	0.138\,02
L_{16}	0.133\,288	0.133\,31	0.133\,39
L_{17}	0.129\,019	0.129\,059	0.129\,19
L_{18}	0.125\,111	0.125\,172	0.125\,36
L_{19}	0.121\,515	0.121\,601	0.121\,85
L_{20}	0.118\,193	0.118\,305	0.118\,63

shown in Fig. 21 plotted on a log-log scale. The figure clearly shows a power law behavior $L_n \sim n^{-\alpha}$ with $\alpha = 0.521\,281$. Here, α is computed by fitting a line through the last two data points corresponding to $n = 21$, $n = 22$. The value should be compared to the asymptotic value described earlier, $\alpha = 0.5$, valid in the limit $n \to \infty$. As n gets large, it is increasingly difficult to compute the periodic orbits, since the particle motion is very near the vortex center and consecutive L_n values converge. For this reason, it is useful to derive a formula that can predict these values. To this end, we define the function $F(n)$ as

$$F(n) = \frac{L_{n-1} - L_n}{L_n - L_{n+1}} \ . \tag{A4}$$

Hence, $F(n)$ represents the ratio of consecutive distances between neighboring L_n values. Using the power law form $L_n \sim n^{-\alpha}$ gives

$$F(n;\alpha) = \frac{(n-1)^{-\alpha} - n^{-\alpha}}{n^{-\alpha} - (n+1)^{-\alpha}} \approx 1 + \frac{(\alpha+1)}{n} + O\left[\frac{1}{n^2}\right] \ . \tag{A5}$$

We can then solve for L_{n+1} in terms of L_n and L_{n-1} to get

$$L_{n+1} = \left[1 + \frac{1}{F(n;\alpha)}\right] L_n - \frac{L_{n-1}}{F(n;\alpha)} \ . \tag{A6}$$

The accuracy of the above formula for a given value of n will depend on our choice of α, but is surprisingly accurate even if we choose the limiting value of $\alpha = 0.5$. For example, using the numerically computed values

$L_{13} = 0.14893$ and $L_{14} = 0.14316$, we compare the predicted values of L_{15} through L_{20} with their numerically computed values in Table I.

For a given value of D, there will be a critical distance L_T so that for an initial distance $L > L_T$ a particle will escape the influence of the vortex around which it orbits. Hence, for the value $D = 0.8$ shown in Fig. 20, there is no L_6 orbit. Particles starting this far from the vortex center enter the chaotic region. The transition value L_T

can be determined computationally, since it corresponds to the initial particle position whose trajectory exactly crosses the center stagnation point. Hence, one can interpret L_T as a crude measure of the "size" of the periodic or quasiperiodic zone. The plot of L_T versus D is shown in Fig. 22. The figure shows power law behavior for $0.2 \leq D \leq 0.9$ with $L_T \sim D^\beta$, where $\beta = 0.569894$ is computed by fitting a least squares line through the data points on a log-log plot.

[1] J. H. Konrad, Caltech Report CIT-8-PU, 1976 (unpublished). This report describes an experimental investigation of mixing in two-dimensional turbulent shear flows with applications to diffusion limited chemical reactions.

[2] R. Breidenthal, J. Fluid Mech. **109**, 1 (1981).

[3] L. S. Huang and C. M. Ho, J. Fluid Mech. **210**, 475 (1990).

[4] Y. Zohar, Ph.D. thesis, University of Southern California, 1990.

[5] C. D. Winant and F. K. Browand, J. Fluid Mech. **63**, 237 (1974).

[6] L. P. Bernal, Ph.D. thesis, California Institute of Technology, 1981.

[7] G. M. Corcos and S. J. Lin, J. Fluid Mech. **139**, 67 (1984).

[8] S. J. Lin and G. M. Corcos, J. Fluid Mech. **141**, 139 (1984).

[9] L. P. Bernal and A. Roshko, J. Fluid Mech. **170**, 499 (1986).

[10] W. T. Ashurst and E. Meiburg, J. Fluid Mech. **189**, 87 (1988).

[11] J. C. Lasheras and H. Choi, J. Fluid Mech. **189**, 53 (1988).

[12] R. D. Moser and M. M. Rogers, Phys. Fluids A **3**, 1128 (1991).

[13] R. D. Moser and M. M. Rogers, J. Fluid Mech. **247**, 275 (1993).

[14] C. Martel, J. Mora, and E. Jimenez, Bull. Am. Phys. Soc. **34**, 2268 (1989).

[15] M. M. Koochesfahani and P. E. Dimotakis, J. Fluid Mech. **170**, 83 (1986).

[16] D. Beigie, A. Leonard, and S. Wiggins, Phys. Fluids A **3**, 1039 (1991).

[17] V. Rom-Kedar, A. Leonard, and S. Wiggins, J. Fluid Mech. **214**, 347 (1990).

[18] M. Hénon, in *Chaotic Behavior of Deterministic Systems*, 1981 Les Houches Lectures, edited by G. Iooss, R. Helleman, and R. Stova (North-Holland, Amsterdam, 1983).

[19] A. J. Lichtenberg and M. A. Liebermann, *Regular and Chaotic Dynamics*, Applied Mathematics and Science Vol. 38 (Springer, New York, 1992).

[20] A. Leonard, J. Comput. Phys. **37**, 289 (1980).

[21] Y. Nakamura, A. Leonard, and P.R. Spalart, AIAA Paper No. 82-0948, 1982 (unpublished).

[22] L. P. Wang and M. R. Maxey, in *Workshop on Mixing in Geophysical Flows—Effects of Body Forces in Turbulent Flows*, edited by J. M. Redondo and O. Metais (Universitat Politecnica de Catalunya, Barcelona, 1992).

[23] A. Michalke, J. Fluid Mech. **19**, 543 (1964).

[24] S. Balachandar and M. Maxey, J. Comput. Phys. **83**, 96 (1989).

[25] E. Meiburg and P. K. Newton, J. Fluid Mech. **227**, 211 (1991).

[26] K. J. Nygaard and A. Glezer, J. Fluid Mech. **231**, 257 (1990).